Martian dust storm impact on atmospheric H2O and D/H observed by ExoMars Trace Gas Orbiter

Ann Carine Vandaele, Daria Betsis, Yuriy S. Ivanov, Bojan Ristic, Håkan Svedhem, Jorge L. Vago, José-Juan López-Moreno, Giancarlo Bellucci, Gustavo Alonso-Rodrigo, Shohei Aoki, et al.

Martian dust storm impact on atmospheric H_2O and D/H observed by ExoMars Trace Gas Orbiter

Journal Item

Version: Accepted Manuscript

Link(s) to article on publisher's website:
http://dx.doi.org/doi:10.1038/s41586-019-1097-3

ExoMars Trace Gas Orbiter observes atmospheric dust, H_2O and HDO during the 2018 dust storm

Ann Carine Vandaele[1], Oleg Korablev[2], Frank Daerden[1], Shohei Aoki[1], Ian R. Thomas[1], Francesca Altieri[3], Miguel López-Valverde[4], Geronimo Villanueva[5], Giuliano Liuzzi[5], Michael D. Smith[5], Justin Erwin[1], Loïc Trompet[1], Anna A. Fedorova[2], Franck Montmessin[6], Alexander Trokhimovskiy[2], Denis Belyaev[2], Nikolay Ignatiev[2], Mikhail Luginin[2], Kevin S. Olsen[6], Lucio Baggio[6], Juan Alday-Pajero[7], Jean-Loup Bertaux[2,6], Daria Betsis[2], David Bolsée[1], Todd Clancy[8], Ed Cloutis[9], Cédric Depiesse[1], Bernd Funke[4], Maia Garcia-Comas[4], Jean-Claude Gérard[10], Marco Giuranna[3], Francisco Gonzalez-Galindo[4], Alexey Grigoriev[2], Yuriy S. Ivanov[11], Jacek Kaminski[12], Ozgur Karatekin[13], Frank Lefèvre[6], Stephen Lewis[14], Manuel López-Puertas[4], Arnaud Mahieux[1], Igor Maslov[2], Jon Mason[14], Michael J. Mumma[5], Lori Neary[1], Eddy Neefs[1], Andrey Patrakeev[2], Dmitry Patsaev[2], Bojan Ristic[1], Séverine Robert[1], Frédéric Schmidt[15], Alexey Shakun[2], Nicholas A. Teanby[16], Sébastien Viscardy[1], Yannick Willame[1], James Whiteway[17], Valérie Wilquet[1], Michael J. Wolff[8], Giancarlo Bellucci[3], Manish R. Patel[14], Jose-Juan Lopez-Moreno[4], François Forget[18], Colin Wilson[7], Håkan Svedhem[19], Jorge L. Vago[19], Daniel Rodionov[2], and the NOMAD and ACS teams

1 Royal Belgian Institute for Space Aeronomy, Brussels, Belgium

2 Space Research Institute (IKI), RAS, Moscow, Russia

3 Istituto di Astrofisica e Planetologia Spaziali (IAPS/INAF), Via del Fosso del Cavaliere, 00133 Rome, Italy

4 Instituto de Astrofisica de Andalucia (IAA/CSIC), Granada, Spain

5 NASA Goddard Space Flight Center, Greenbelt, MD, USA

6 LATMOS, UVSQ Université Paris-Saclay, Sorbonne Université , CNRS, France

7 Physics Department, Oxford University, OX1 3PU Oxford, UK

8 Space Science Institute, 4750 Walnut St, Suite 205, Boulder, Colorado, 80301, USA

9 Department of Geography, University of Winnipeg, Winnipeg, Manitoba, Canada R3B 2E9

10 LPAP, University of Liege, Liège, Belgium

11 Main Astronomical Observatory MAO NASU, Kyiv, Ukraine

12 Institute of Geophysics, Polish Academy of Sciences, Warsaw, Poland

13 Royal Observatory of Belgium, av. Circulaire 3, 1180 Brussels, Belgium

14 School of Physical Sciences, The Open University, Walton Hall, Milton Keynes, MK7 6AA, U.K.

15 GEOPS, Univ. Paris-Sud, CNRS, Université Paris-Saclay, Rue du Belvédère, Bât. 504-509, 91405 Orsay, France

16 School of Earth Sciences, University of Bristol, Wills Memorial Building, Queens Road, Bristol, BS8 1RJ, UK

17 Centre for Research in Earth and Space Science, York University, Toronto, Ontario, Canada

18 LMD, CNRS Jussieu, Paris, France

19 European Space Agency, Noordwijk, the Netherlands

Global dust storms develop at Mars at irregular intervals of several years[1,2]. They have major effects, causing an inflation of the atmosphere and changes in the dynamical behaviour, primarily due to solar heating of the dust. Recently published observations of Mars' atmospheric water abundance during dust storm conditions revealed a high-altitude increase, more pronounced at high northern latitudes[3,4], and a decrease in the water column at low latitudes[5,6]. These results, however, lacked concurrent measurements of atmospheric dust loading[3], had a poor vertical resolution[3], or were indirect[4]. The start of science operations with the ESA/ROSCOSMOS ExoMars Trace Gas Orbiter spacecraft coincided with the onset of a global dust storm on Mars. We provide new evidence of the

impact of this dust storm on the vertical distribution of dust and water vapour. Also, for the first time, the vertical distribution of the HDO/H_2O ratio is determined from high spectral resolution solar occultation measurements of water – H_2O and HDO – obtained simultaneously by both NOMAD[7] and ACS[8]. Before the storm, HDO abundances drop below detectability at 40-45 km altitude. This decrease in HDO is shown to be correlated with the presence of H_2O ice clouds. During the storm, higher abundances of both H_2O and HDO are observed above 40 km and up to 60-80 km. These increased abundances are a result of the warmer temperatures during the dust storm, causing a stronger atmospheric circulation and preventing cloud formation. The transition was sudden and occurred in 1-2 days while the dust storm was developing, indicating a swift atmospheric reaction to the dust storm.

Although dust is ubiquitous in Mars' atmosphere, global-scale dust storms (GDS) are relatively rare events[1,2] which only occurred twice in the last 17 years (in 2001 and 2007). The effects of such global storms on the Martian atmosphere can last several months. The physical processes responsible for these phenomena are not yet fully understood, although several mechanisms have been proposed[9]. The ExoMars Trace Gas Orbiter (TGO) arrived at Mars in October 2016 and started its first science observations in April 2018, just before the beginning of the 2018 global dust storm. The NOMAD[7] and ACS[8] instruments on board TGO witnessed the onset and development of this global dust storm and its impact on water vapour abundance in the Martian atmosphere.

The 2018 GDS started on 30 May near the northern autumn equinox (L_s~185°) and, within a few weeks, the planet was covered with atmospheric dust. Instruments on other Mars-orbiting and landed spacecraft also witnessed the storm's evolution (e.g. PFS and VMC[10] on board Mars Express, MARCI and MCS[11] on Mars Reconnaissance Orbiter and THEMIS[12] on Mars Odyssey). Observations by Curiosity[13] in Gale Crater indicated that the dust opacity rose from 0.65 on 7 June to 6.7 on 24 June,

consistent with the values found by NOMAD and ACS which observed dust opacity to increase by a factor larger than 10 (see Methods).

TGO has a 2-hour orbit and can perform atmospheric measurements during two solar occultation events per orbit when the geometry is favourable. The NOMAD and ACS instruments measure the solar radiation spectrum that is filtered by the atmosphere and from which the vertical distribution of atmospheric compounds, in particular water vapour (both isotopologues, H_2O and HDO), can be retrieved. Atmospheric opacity variation with altitude can also be obtained directly from the decrease in the continuum part of the transmitted solar intensity, thus allowing the instruments to monitor the onset and further evolution of the dust storm (Figure 1).

In solar occultation mode, while the TGO-to-Sun line of sight sweeps tangent altitudes above the top of the atmosphere, the sampled line-of-sight optical depth is zero (*i.e.,* no attenuation of the solar signal). When the line of sight to the Sun transects the atmosphere, the line-of-sight optical depth gradually increases, owing to the presence of dust and ice particles, until the atmosphere becomes completely opaque at some tangent altitude. Here the transmittance drops to zero and the line-of-sight optical depth increases to infinity, which usually occurs due to enhanced dust presence in the lowermost part of the atmosphere or, in rarer cases, by the planetary surface. Dust and/or cloud layers in the atmosphere cause local increases in optical depth, with the effect being most pronounced in the equatorial region (Figure 1.D-F). The characteristics of the individual vertical profiles of optical depth vary with latitude before, during and after the dust storm.

The observations in Figure 1.A-C were made north of 60° latitude, and indicate that the continuum line-of-sight optical depth remains low down to 10-20 km tangent altitude throughout the dust storm. The apparent increase with time of the tangent altitude at which the atmosphere becomes opaque is mainly a latitude effect, indicating that the global dust storm does not impact much the

104 northern latitudes. Some features at 25-40 km altitude were observed from June onwards that were
105 not present before the dust storm: these could be layers of dust that are transported from lower
106 latitudes.
107
108 In the mid-latitudes (Figure 1.D-F), before the dust storm, many layers were observed around 40 km.
109 Detached dust layers were previously identified on many occasions[14-16], and their existence has been
110 explained by uplifting during strong convection processes[17-20]. Water ice clouds may be responsible
111 for some of the observed layers, as indicated by observations at other wavelengths and by previous
112 investigations[21-23]. The layers disappear during the dust storm when the atmosphere is utterly
113 opaque below 40 km because of high dust abundances, and water ice clouds are expected to
114 disappear due to the atmospheric warming in the dust storm[14].
115
116 Furthemore, Figure 1.G-I shows the impact of dust/ice clouds in the high southern latitudes, from
117 the beginning of southern spring to the onset of the dusty southern summer season. During the GDS,
118 dust ascended to higher altitudes, comparable to the situation in the mid-latitudes but with more
119 local variability.
120
121 On Mars, water vapour has a wide variety of effects on atmospheric photochemistry and climate. Its
122 dissociation by sunlight into hydroxyl radicals controls the overall stability cycle of CO_2. As frost on
123 the surface or as ice clouds in the atmosphere, water exerts a strong influence, leading to large
124 departures from the otherwise dust-controlled radiative balance[24].
125
126 Here we present the first water vapour profiles that reach down to the planetary boundary layer,
127 with a high vertical resolution (~1 km) and extent up to ~80 km (Figure 2 and Figure 3.A). Besides,
128 for the first time, the vertical profile of HDO could be measured (Figure 3.B). The first observations
129 from TGO were carried out prior to the 2018 GDS, and the impact of the global dust storm on the

vertical distribution of water vapour and HDO could be monitored. The ACS observations shown in Figures 2 and 3 were performed at high southern and northern latitudes, while the NOMAD profiles were obtained in northern mid-latitudes. During the northern autumnal season, when these measurements were carried out, previous column-integrated measurements[5,6] indicated a dry atmosphere at high latitudes caused by the developing seasonal polar cap in the North and its receding counterpart in the South. The seasonal cap development therefore explains the very low water abundances in the lowest 20 km for the sub-polar profiles (Figure 2). The profiles observed before the dust storm indicate low abundances of water vapour above 60 km, with values below 10 ppm, and with large error bars. Profiles from the southern hemisphere are shown in Figure 2(Right) and Figure 3.A; they correspond to the southern summer season with a lot of dust present in the atmosphere already before the GDS, explaining the lack of data below ~15 km. Northern hemisphere profiles were taken in more dust-free conditions and reach down to ~4 km.

Water profiles, both H_2O and HDO, show a large enhancement in the middle atmosphere after the onset of the dust storm. The increase in water abundance is observed above 20 km, with water vapour being lifted upwards up to at least 80 km. Previous studies have reported a sharp decrease of the total water column in the equatorial region[5,6], indicative of redistribution of water vapour in a dust storm. Previous measurements[3] of water vapour profiles already exhibited an increase of the atmospheric water content at high altitudes and latitudes, as is confirmed by these new data. This phenomenon was also linked to an increase in the escape of hydrogen from Mars' atmosphere[4,25]. What is remarkable in the observations presented here (Figure 2), is that this enhancement is happening very fast, in the course of just a few days during the onset of the dust storm (around 7-8 June, Ls~188-190°).

The observed changes in the distribution of atmospheric water reported here can be understood as resulting from a variety of processes. The higher abundance of dust heats large parts of the

156 atmosphere because of the absorption of solar radiation by the dust particles. Dust absorption and
157 subsequent warming of surrounding gas causes an expansion of the atmosphere, which leads to a
158 redistribution of water vapour to a wider vertical range. The higher atmospheric temperatures at
159 low and middle latitudes and the resulting higher thermal contrast between the equatorial and polar
160 regions also strengthen the mean meridional circulation, this leads to an additional redistribution of
161 water vapour across latitude. Also because of the higher temperatures, fewer water ice clouds are
162 expected to be present during a dust storm. Under normal conditions, the formation of clouds acts
163 to confine water vapour to lower altitudes due to the gravitational fall and subsequent sublimation
164 of ice crystals. In addition, numerical modelling has also demonstrated that solar heating of
165 atmospheric dust can drive localized deep convection[18,19] and larger scale ascent of dust layers[20] that
166 would, along with the dust, also transport water vapour to higher altitudes. All these processes that
167 contribute to explaining the observed changes in the water vapour profiles have been quantitatively
168 demonstrated with global circulation models (GCMs) and by data assimilation of water vapour in
169 previous years on Mars[24,26-28]. For a more quantitative understanding of the 2018 GDS, more detailed
170 modelling and assimilation studies that simulate the transition from normal to global dust storm
171 conditions[24,26,27,29] will have to be performed, using dust constraints derived from instruments that
172 monitored the GDS, including TGO instruments.
173
174 The fractionation between H_2O and HDO is an important process in planetary atmospheres. The D/H
175 ratio is a marker of the evolution of the water inventory on Mars[30]. On this planet, the D/H budget is
176 dominated by H_2O and HDO which are the unique precursors of the escaping D and H atoms above
177 the exobase. HDO was previously measured as column-integrated abundances from Earth[31-33] and *in*
178 *situ*[34] by the Mars Science Laboratory. NOMAD and ACS provide for the first time the capability to
179 observe the vertical distribution of HDO simultaneously with water vapour, thereby providing key
180 information on the fractionation processes that are expected to control the amount of hydrogen and
181 deuterium atoms escaping to space[25]. H_2O and HDO are fractionated during photolysis and ice

formation[35]. The fractionation during ice formation is expected to reduce the D/H ratio above the hygropause and keep HDO more strongly confined in the lower atmosphere. Indeed, condensation will enhance D/H in ice particles, that sediment and subsequently sublimate, preventing HDO even more than H_2O to reach higher altitudes.

NOMAD observations (Figure 3) reveal that the HDO density profiles during the pre-storm period exhibit a sudden decline at 40-45 km altitude, just below a thick layer of water ice clouds, consistent with this view (see Methods and Figure 9). ACS observations show this decrease to occur at 50 km but were taken at a different latitude, where the hygropause may be located at a different altitude. Moreover, ACS data have larger error bars near the top of the profile. The HDO/H_2O ratio is similar in both profiles below 45 km: 4-6 VSMOW. HDO is distinctly more abundant at high altitudes during the dust storm than before the storm. This is explained by the strong atmospheric warming during the GDS, which causes the hygropause to ascend to higher altitudes. The HDO/H_2O ratio is relatively similar before and during the GDS, which demonstrates that HDO is advected along with H_2O to higher altitudes and latitudes during the onset of the GDS.

The first observations of H_2O and HDO, leading to the determination of vertical profiles of D/H, have shown that these two species are very sensitive to the presence of ice clouds which suppress them and prevent them to reach the atmospheric layers above the clouds. This fractionation-based mechanism was theoretically predicted by models for a long time but never demonstrated[35]. The effect of the dust storm is to expand the atmosphere and to lift the hygropause. Continued measurements by TGO shall permit us to unveil both the spatial and the seasonal trends of D/H.

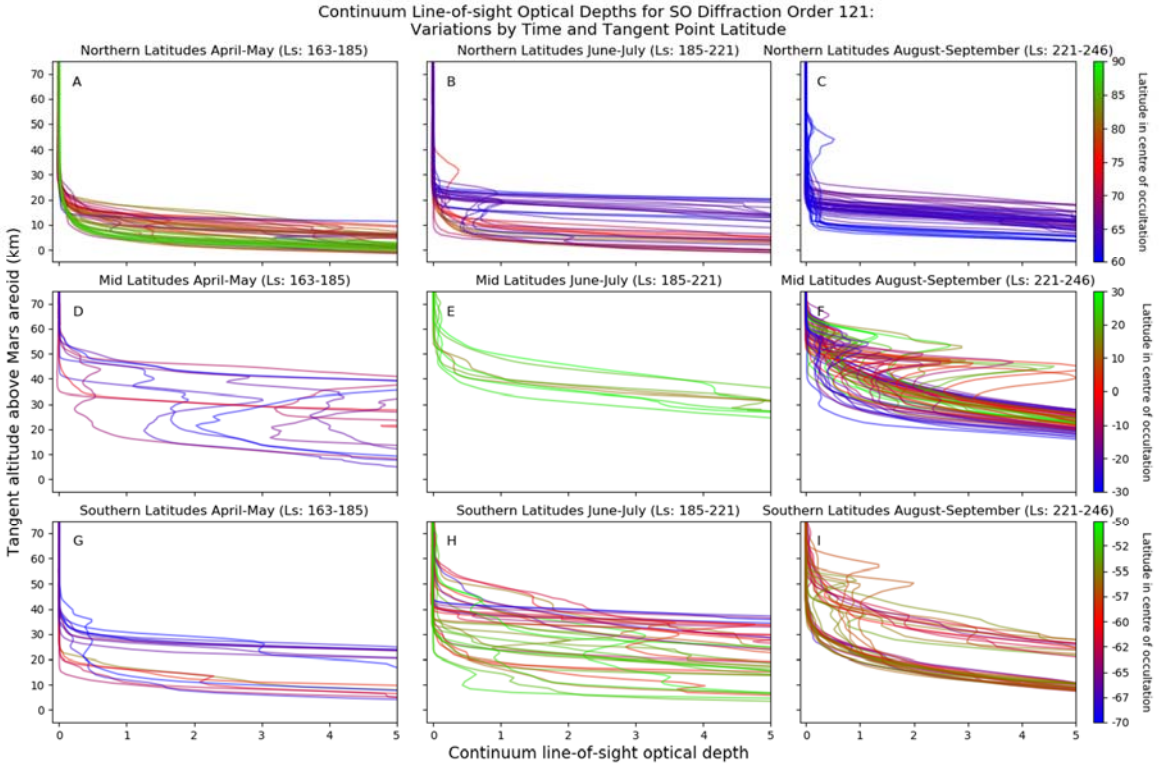

Figure 1: Evolution of the dust/cloud extinction obtained by the NOMAD SO channel during the onset of the global dust storm: from the first observations in April and May (left panels) to the August-September 2018 timeframe (right panels), spanning Ls = 163° to 246° (late northern summer to autumn). The data is split into 3 latitude bins, with the colour of the line indicating the latitude within each bin. The latitudinal coverage is dependent on the orbit and solar position, and so the latitude ranges were selected based on the data available: northern profiles for latitude > 60°N (upper panels); mid-latitude profiles for latitudes between -30°S and 30°N (middle panels); and southern profiles for latitudes between -70°S and -50°S (lower panels). In the early phase of the TGO mission, more solar occultations occurred near the northern pole, as is evident in the figures. Plotted here is the continuum line-of-sight optical depth versus tangent altitude of the centre of the line of sight above the Mars reference areoid. The line-of-sight optical depth is inferred from the transmittance after the removal of atmospheric absorption lines. Diffraction order 121 was used for this study, covering the 2720-2740 cm^{-1} spectral range. Horizontal error bars are not shown here, as they are very small (0.003 units for optical depth = 1; 0.06 units for optical depth = 4; for an SNR of 1000).

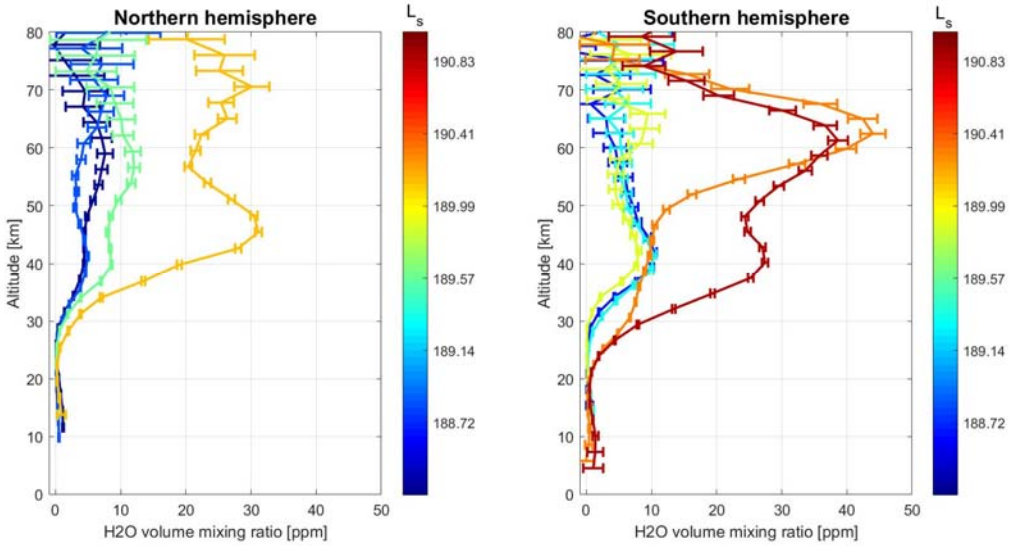

Figure 2: H_2O volume mixing ratio (vmr) profiles observed by ACS NIR, during the onset of the global dust storm . Left: northern latitudes; black: Ls = 188.28° – Lat = 77.5° N; blue: Ls = 188.75° – Lat = 76.4° N; green: Ls = 189.41° – Lat = 74.8° N; yellow: Ls = 189.90° – Lat = 73.8° N. Right: southern latitudes; blue: Ls = 188.62° – Lat = 68.2° S; cyan: Ls = 189.19° – Lat = 70.0° S; yellow: Ls = 189.67° – Lat = 71.3° S; orange: Ls = 190.05° – Lat = 72.4° S; red: Ls = 190.50° – Lat = 73.8° S. Water abundances were deduced from ACS NIR observations (order 56 covering the 1.38 µm band, 7225-7300 cm^{-1}; the CO_2 density was measured in order 49, 6320-6390 cm^{-1}).

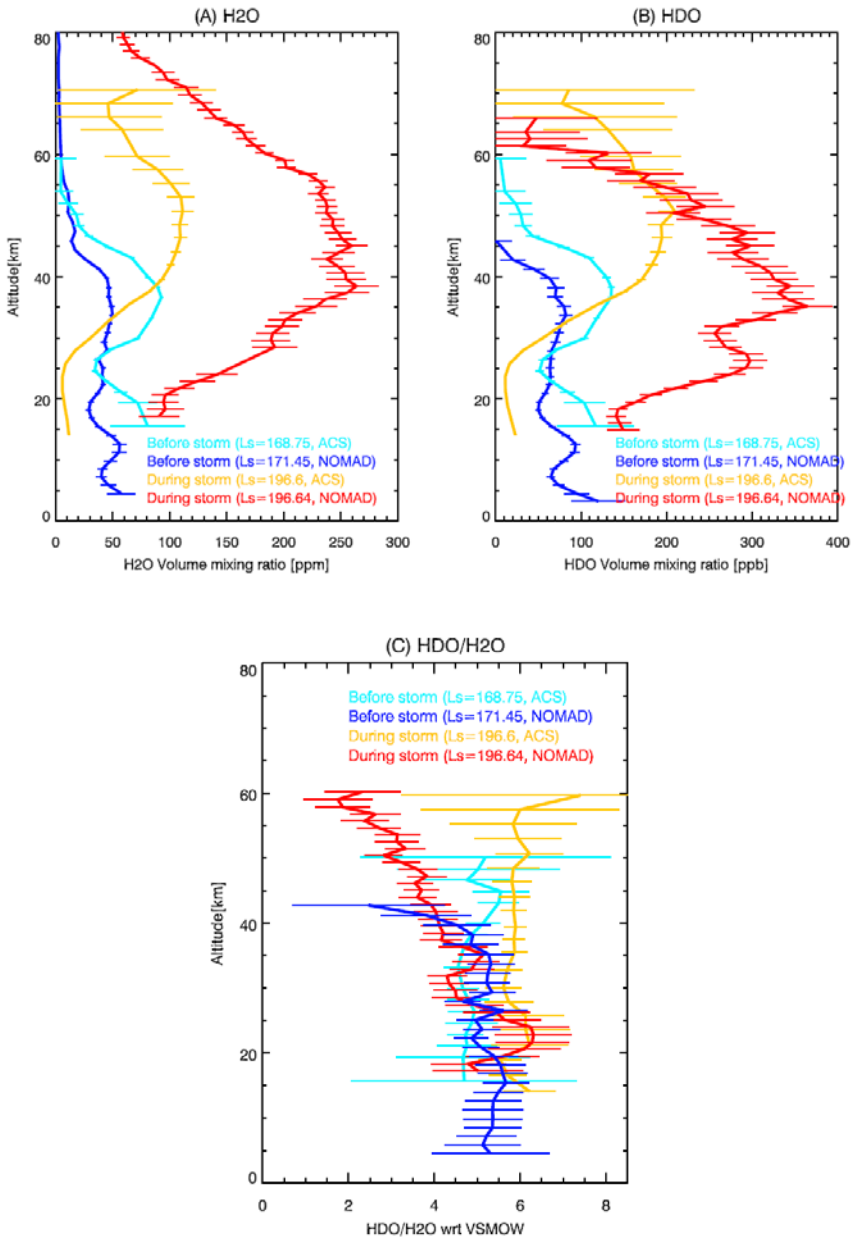

Figure 3: H_2O, HDO and D/H detections before and during the storm. Panel A: NOMAD H_2O observations before the storm (blue: Ls: 171.45°, Lat: 43°N to 68°N), and during the storm (red: Ls: 196.64°, Lat: 51°N to 59°N,) and ACS MIR observations before the storm (cyan: Ls: 168.75°, Lat: 39°S to 43°S), and during the storm (yellow: Ls: 196.64°, Lat: 80°S to 83°S). The corresponding HDO VMR profiles are shown in Panel B. Panel C shows the D/H ratio obtained for each of the H_2O-HDO observations. All errors in Panel A–C are 1σ. VSMOW is the Vienna Standard Mean Ocean Water reference value, 312 ppm HDO/H_2O.

References

1 Shirley, J. H., Newman, C., Mischna, M. & Richardson, M. Replication of the historic record of martian global dust storm occurrence in an atmospheric general circulation model. *Icarus* **317**, 197-208, doi:https://doi.org/10.1016/j.icarus.2018.07.024 (2019).

2 Montabone, L. *et al.* Eight-year climatology of dust optical depth on Mars. *Icarus* **251**, 65-95 (2015).

3 Fedorova, A. *et al.* Water vapor in the middle atmosphere of Mars during the 2007 global dust storm. *Icarus* **300**, 440-457 (2018).

4 Heavens, N. G. *et al.* Hydrogen escape from Mars enhanced by deep by deep convection in dust storms. *Nature Letters* **2**, 126-132, doi:10.1038/s41550-017-0353-4 (2018).

5 Smith, M., Daerden, F., Neary, L. & Khayat, A. The climatology of carbon monoxide and interannual variation of water vapor on Mars as observed by CRISM and modeled by the GEM-Mars general circulation model. *Icarus* **301**, 117-131, doi:https://doi.org/10.1016/j.icarus.2017.09.027 (2018).

6 Trokhimovsky, A. *et al.* Mars' water vapor mapping by the SPICAM IR spectrometer: Five martian years of observations. *Icarus* **251**, 50-64 (2015).

7 Vandaele, A. C. *et al.* NOMAD, an integrated suite of three spectrometers for the ExoMars Trace Gas mission: technical description, science objectives and expected performance. *Space Sci. Rev.* **214:80**, doi.org/10.1007/s11214-11018-10517-11212, doi:https://doi.org/10.1007/s11214-018-0517-2 (2018).

8 Korablev, O. *et al.* The Atmospheric Chemistry Suite (ACS) of three spectrometers for the ExoMars 2016 Trace Gas Orbiter. *Space Sci. Rev.* **214: 7**, https://doi.org/10.1007/s11214-11017-10437-11216 (2018).

9 Kahre, M. *et al.* in *The atmosphere and climate of Mars Cambridge Planetary Science* (eds R.M. Haberle *et al.*) 229-294 (Cambridge University Press, 2017).

10 Sanchez-Lavega, A. *et al.* in *AGU Fall Meeting 2018.*

11 Schoffield, J. T., Kleinbohl, A., Kass, D. & McCleese, D. in *42nd COSPAR Scientific Meeting* (Pasadena, CA, USA, 14-22 July, 2018).

12 Smith, M. D. in *AGU Fall Meeting 2018.*

13 Vasada, A., Crisp, J. & Meyer, M. in *42nd COSPAR Scientific Meeting* (Pasadena, CA, USA, 14-22 July, 2018).

14 Guzewich, S., Talaat, E., Toigo, A., Waugh, D. W. & McConnochie, T. High-altitude dust layers on Mars: Observations with the Thermal Emission Spectrometer. *J. Geophys. Res. Planets* **118**, 1177–1194, doi:doi:10.1002/jgre.20076 (2013).

15 Heavens, N. G. *et al.* Seasonal and diurnal variability of detached dust layers in the tropical Martian atmosphere. *J. Geophys . Res .: Planets* **119**, 1748-1774, doi:10.1002/2014JE004619 (2014).

16 Määttänen, A. *et al.* A complete climatology of the aerosol vertical distribution on Mars from MEx/SPICAM UV solar occultations. *Icarus* **223**, 892-941, doi:http://dx.doi.org/10.1016/j.icarus.2012.12.001 (2013).

17 Wang, C. *et al.* Parameterization of Rocket Dust Storms on Mars in the LMD Martian GCM: Modeling Details and Validation. *J. Geophys . Res .* **123**, 982-1000, doi:https://doi.org/10.1002/2017JE005255 (2018).

18 Rafkin, S. The potential importance of non-local, deep transport on the energetics, momentum, chemistry,and aerosol distributions in the atmospheres of Earth, Mars, and Titan. *Planetary and Space Science* **60**, 147-154, doi:10.1016/j.pss.2011.07.015 (2012).

19 Spiga, A., Faure, J., Madeleine, J. B., Maattanen, A. & Forget, F. Rocket dust storms and detached dust layers in the Martian atmosphere. *J. Geophys . Res .* **118**, 746-767, doi:10.1002/jgre.20046 (2013).
20 Daerden, F. *et al.* A Solar Escalator on Mars: Self-Lifting of Dust Layers by Radiative Heating. *Geophys. Res. Lett.* **42**, 7319–7326, doi:doi:10.1002/2015GL064892 (2015).
21 Clancy, R. T. *et al.* Extension of atmospheric dust loading to high altitudes during the 2001 Mars dust storm: MGS TES limb observations. *Icarus* **207**, 98-109 (2010).
22 Sefton-Nash, E. *et al.* Climatology and first-order composition estimates of mesospheric clouds from Mars Climate Sounder limb spectra. *Icarus* **222**, 342-356, doi:https://doi.org/10.1016/j.icarus.2012.11.012.
23 McCleese, D. J. *et al.* Structure and dynamics of the Martian lower and middle atmosphere as observed by the Mars Climate Sounder: Seasonal variations in zonal mean temperature, dust, and water ice aerosols. *J. Geophys. Res.* **115**, E12016, doi:doi:10.1029/2010JE003677 (2010).
24 Montmessin, F., Smith, M. D., Langevin, Y., Mellon, M. & Fedorov, A. in *The atmosphere and climate of Mars Cambridge Planetary Science* (eds R.M. Haberle *et al.*) 229-294 (Cambridge University Press, 2017).
25 Chaffin, M. S., Deighan, J., Schneider, N. M. & Stewart, A. I. F. Elevated atmospheric escape of atomic hydrogen from Mars induced by high-altitude water. *Nature Geoscience* **10**, 174-178, doi:DOI: 10.1038/NGEO2887 (2017).
26 Forget, F. *et al.* Improved general circulation models of the Martian atmosphere from the surface to above 80 km. *J. Geophys . Res .* **104**, 24155-24175 (1999).
27 Neary, L. & Daerden, F. The GEM-Mars General Circulation Model for Mars: Description and Evaluation. *Icarus* **300**, 458–476, doi:https://doi.org/10.1016/j.icarus.2017.09.028 (2018).
28 Steele, L. *et al.* The seasonal cycle of water vapour on Mars from assimilation of Thermal Emission Spectrometer data. *Icarus* **237**, 97-115, doi:http://dx.doi.org/10.1016/j.icarus.2014.04.017 (2014).
29 Lewis, S. R. *et al.* The solsticial pause on Mars: 1. A planetary wave reanalysis. *Icarus* **264**, 456-464, doi:https://doi.org/10.1016/j.icarus.2015.08.039 (2016).
30 Lammer, H. *et al.* Outgassing History and Escape of the Martian Atmosphere and Water Inventory. *Space Sci. Rev.* **174**, 113-154 (2013).
31 Encrenaz, T. *et al.* New measurements of D/H on Mars using EXES aboard SOFIA. *Astron. Astrophys.* **612**, A112 (2018).
32 Aoki, S. *et al.* Seasonal variation of the HDO/H_2O ratio in the atmosphere of Mars at the middle of northern spring and beginning of northern summer. *Icarus* **260**, 7-22, doi:http://dx.doi.org/10.1016/j.icarus.2015.06.021 (2015).
33 Villanueva, G. *et al.* Strong water isotopic anomalies in the martian atmosphere: Probing current and ancient reservoirs. *Science* **348**, 218-221 (2015).
34 Webster, C. R. *et al.* Isotope Ratios of H, C and O in CO_2 and H_2O of the Martian Atmosphere. *Science* **341**, 260-263, doi:10.1126/science.1237961 (2013).
35 Montmessin, F., Fouchet, T. & Forget, F. Modeling the annual cycle of HDO in the Martian atmosphere. *J. Geophys. Res.* **110**, doi:10.1029/2004JE002357 (2005).

Methods

The NOMAD instrument and dataset. NOMAD, the "Nadir and Occultation for MArs Discovery" spectrometer suite[7,36,37], is part of the payload of the ExoMars 2016 Trace Gas Orbiter mission[38]. The instrument is conducting a spectroscopic survey of Mars' atmosphere in ultraviolet (UV), visible and infrared (IR) wavelengths covering large parts of the 0.2-4.3 μm spectral range. NOMAD is composed of three spectrometers: a solar-occultation-only spectrometer (SO – Solar Occultation) operating in the infrared (2.3-4.3 μm), a second infrared spectrometer (2.3-3.8 μm) capable of nadir, but also solar occultation and limb observations (LNO – Limb Nadir and solar Occultation), and an ultraviolet/visible spectrometer (UVIS – UV visible, 200-650 nm) that also has all three observation modes. The spectral resolution of SO (0.15 cm^{-1} at 3000 cm^{-1}) surpasses previous surveys from orbit in the infrared by at least one order of magnitude. NOMAD offers an integrated instrument combining a flight-proven concept and innovations based on existing instrumentation: SO is a copy of the Solar Occultation in the IR (SOIR) instrument[39] on Venus Express (VEx[40]), LNO is a modified version of SOIR, and UVIS has heritage from the development in the context of the Humboldt lander. NOMAD provides vertical profiling for atmospheric constituents at unprecedented spatial and temporal resolution. Indeed, in solar occultation, the vertical resolution is less than 1 km for SO and UVIS, with a sampling rate of 1 s (one measurement every 1 km), and occultations range from the surface to 200 km altitude. NOMAD also provides mapping of several constituents in nadir mode with an instantaneous footprint of 0.5 x 17 km^2 (LNO spectrometer) and 5 km^2 (UVIS spectrometer), with a repetition rate of 30 Martian days.

For this work we analysed SO channel data measured between April 21st and September 30th. SO measures 4 spectra for 5 or 6 different diffraction orders per second.

The ACS instrument and dataset. ACS[8] consists of three infrared channels featuring high accuracy, high resolving power, and a broad spectral coverage (0.7 to 17 μm). The near-infrared (NIR) channel is based on the principle of echelle-spectrometer with selection of diffraction orders by an acousto-optical tuneable filter (AOTF). The same principle was employed by SOIR on VEx[4] and by the infrared channels of NOMAD described above. ACS NIR covers a spectral range of 0.7-1.7 μm in diffraction orders 101 through 49. The instrument capitalises at the science heritage of SPICAM-IR[41] on board ESA's Mars Express, benefiting from much higher resolving power of $\lambda/\Delta\lambda \approx 25{,}000$. During an occultation, ACS NIR measures 10 preselected diffraction orders in two seconds, including the absorption bands of H_2O at 1.13, 1.38, and 1.40 μm, and CO_2 at 1.27, 1.43, 1.54, and 1.57 μm. The mid-infrared (MIR) channel is a newly developed crossed dispersion echelle spectrometer dedicated to solar occultation measurements in the 2.3-4.5 μm range. The spectral resolving power is $\lambda/\Delta\lambda \approx 50{,}000$. For each acquired frame, MIR measures up to 20 adjacent diffraction orders, covering an instantaneous spectral range of 0.15-0.3 μm. To achieve the full spectral coverage a secondary dispersion grating can be rotated to one out of 11 positions. The H_2O and HDO profiles can be measured simultaneously by MIR using the positions 4, 5 and 11.

The concept of Fourier-transform spectrometer TIRVIM is close to that of Planetary Fourier Spectrometer (PFS[42]) on board MEx, though TIRVIM features a cryogenic detector and the solar occultation capability. In occultation, TIRVIM is operated mostly in 'climatology' mode, covering instantaneously, each 0.4 s, the full spectral range of 1.7-17 μm (effectively 1.7-5 μm) with spectral resolution ≤1 cm^{-1}. These three channels are used to observe in solar occultation; NIR and TIRVIM are operated also in nadir to measure atmospheric gases and to characterise the atmospheric state: dust loading and condensation clouds. The atmospheric temperature profile is retrieved from the 15-μm CO_2 band measured by TIRVIM in nadir.

In this work we used NIR occultation profiles (Figure 2) obtained at high latitudes in the southern and northern hemispheres (see Table 1). MIR simultaneous H_2O and HDO profiles (Figure 3) were obtained in the southern hemisphere in order 224 (position 4 of secondary grating). TIRVIM aerosol profiling (Figure 10) was done using solar occultation data obtained in the southern hemisphere, orbit 2556, Ls=197°, latitude 81°S during the egress (local time 9:26), i.e. during the same occultation of the MIR results shown in Figure 3.

Solar occultation technique. The solar occultation technique is a powerful method to gain information on the vertical structure of atmospheres. At sunset, the recording of spectra starts well before the occultation occurs (the solar spectrum outside the atmosphere is used for referencing), and continues until the line of sight crosses the planet. At sunrise, the recording of spectra continues well above the atmosphere to provide the corresponding reference. Transmittances are obtained by dividing the spectra measured through the atmosphere by the reference spectrum recorded outside the atmosphere[43]. In this way, transmittances become independent of instrumental characteristics, such as the absolute response or the ageing of the instrument and, in particular, of the detector. Such observations provide high vertical resolution (< 1 km for NOMAD SO and ACS NIR and 2.0-2.5 km for ACS MIR observations) profiles of the structure and composition of the atmosphere. ACS TIRVIM observes the full Sun disk during an occultation, resulting in a coarser vertical resolution (~9 km).

Profiles of dust extinction. To calculate the extinction due to dust and/or clouds, it is necessary to remove the absorption lines of atmospheric gas species, leaving the background continuum. For the analysis here, diffraction order 121 of NOMAD SO was chosen, as 1) this order is measured routinely, so has high spatial/temporal coverage; and 2) it is relatively simple to remove the atmospheric absorption lines. A 4^{th} order polynomial is fitted to the data. The optical depths in Figure 1 are inferred from the value of the continuum in the centre of the detector (pixel 160). The fitting

algorithm fails at low and high altitudes, where the absorption lines from molecular species are saturated or the signal is so low that it is effectively noise. Therefore, any spectra where transmittance > 99.5% are assumed to have an optical depth of 0, and points where transmittance < 0.5% are not plotted; hence the lines end abruptly at low altitudes when the optical depth becomes high. The observations in Figure 1 are split into North, South and mid-latitudes using the following criteria: greater than 60° North, between -70° and -50° South, and between -30° and +30° for the mid-latitudes. The tangent altitude is calculated as the shortest distance between the line of sight of the centre of the field of view and the MGM1025 Areoid (i.e. the Mars geoid)[44]. The latitude is the point on the areoid closest to the centre of the field of view, i.e. the tangent point, at the midpoint of the solar occultation measurement. The characteristics of the individual vertical profiles of optical depth vary with latitude, as seen when optical depth is plotted vs latitude and Mars longitude (Figure 4).

To further investigate the impact of the dust storm, two orbits covering the same footprint and solar illumination conditions on Mars have been considered; they were acquired by the nadir channel of NOMAD, respectively, before (April 26th) and during (July 11th) the global dust storm. Figure 5 compares the dust radiance signature before and after the storm but, in contrast to Figure 1, now in a nadir geometry and in a different wavelength, at 2.3 μm. Comparison with radiative transfer modelling suggests a factor of ~10 increase in opacity at 2.3 μm during the storm. Note also how the surface albedo features are obscured by the increase of the atmospheric dust load. The radiance variation with latitude is mainly dominated by the total albedo (surface + atmosphere) and solar zenith angle, which varies along the track. The radiative transfer model includes multiple scattering and a layered atmosphere with pressure/temperature profiles from the LMD General Circulation Model[45]. Further details on the radiative transfer model can be found in Villanueva, et al. [46].

Vertical profiles of H_2O and HDO volume mixing ratio. The vertical profiles of H_2O and HDO volume mixing ratio are investigated from the NOMAD dataset shown in Table 1. These NOMAD spectra are all taken in the northern hemisphere at the same local time (at 18h). The NOMAD SO channel can record spectra for multiple diffraction orders during an occultation. The occultation performed on 7 May includes the measurements of diffraction order 168 (3775.53 – 3805.63 cm^{-1}) and order 136 (3056.39 – 3080.75 cm^{-1}) where strong H_2O lines are present and of order 119 (2674.34 – 2695.65 cm^{-1}) with strong HDO lines. The occultation measurement on 20 June contains two diffraction orders for H_2O - order 168 and 134 (3011.44 – 3035.44 cm^{-1}), and diffraction order 121 for HDO (2719.28 – 2740.96 cm^{-1}) (Figure 6).

We retrieved H_2O volume mixing ratio using the whole spectral range of those diffraction orders, in order to maximize the information content at every tangent altitude. In this study, CO_2 and H_2O gas absorptions were included. The absorption coefficients of these gases are calculated based on a line-by-line method using the water vapour line list for a CO_2-rich atmosphere for H_2O[47,48] and HITRAN 2016[49] for CO_2. Temperature, pressure, and CO_2 volume mixing ratio are taken from the values predicted by GCMs for each altitude. The calculated synthetic spectra are convolved with a Gaussian function that corresponds to the spectral resolving power of the NOMAD SO channel (R=11000-15000). The final synthetic spectra are then built by considering an instrument model that comprises the effects of the Acousto-Optic Tunable Filter (AOTF) and the grating (i.e., Blaze function)[50]. The free parameters in the retrievals are the vertical profiles of volume mixing ratio and the parameters for the polynomial function to model the continuum of each spectrum. Retrievals are performed using an Optimal Estimation approach[51] implemented in a Gauss-Newton iterative scheme. Figure 7 shows an example of fit results.

The water vapour profiles shown in Figure 2 are retrieved from the ACS NIR spectra (see also Table 1). Wavelength drift is corrected using positions of gaseous absorption lines. The spectra fitting and

the profile retrieval follow the method described for SPICAM MEx 1.38-µm band[3,52]. All the altitudes of the profiles are fitted simultaneously (global fit) using a Levenberg–Marquardt iterative algorithm[53,54], where Y is a matrix of all spectra changing with altitude and X is a vector of gaseous densities. A Tickhonov regularization is then applied, customary for vertical inversions in order to smooth the profile and minimize the errors. The uncertainty in the local number densities is given by the covariance matrix of the solution errors. The water vapour abundances were retrieved from spectra acquired in diffraction order 56 (covering the 1.38 µm band, or 7220-7300 cm^{-1}). Figure 8 shows an example of fit results. The spectral line parameters for H_2O are taken from HITRAN 2016[49] with a correction coefficient for the CO_2 rich atmosphere[3]. Temperature and pressure for the radiative transfer computations are taken from GCM MCD[45]. To obtain the VMR profiles of water vapour, the CO_2 density was retrieved from ACS NIR spectra in order 49, 6320-6390 cm^{-1}.

The vertical profiles of H_2O and HDO volume mixing ratio investigated from the ACS dataset (Figure 3. B and C) were obtained in the southern hemisphere at middle and high latitudes (Table 1). During these observations MIR channels recorded spectra at position 4 (diffraction orders 210-224). To obtain the H_2O and HDO density, the order 224 (3763-3775 cm^{-1}) was used for both observations in 2th May and 20th June. We retrieved H_2O and HDO volume mixing ratio using several lines present in this diffraction order. The spectral line parameters for H_2O are taken from HITRAN 2016 with a correction coefficient for the CO_2 braodening[3]. Temperature and pressure for radiative transfer computations are taken from GCM MCD[45]. The calculated synthetic spectra are convolved with a Gaussian function that corresponds to the spectral resolving power of the ACS MIR channel (R~30000-35000).

Water ice clouds. Figure 9 shows the aerosol optical depth derived from NOMAD SO on May 7th, 2018 before the dust storm, during which orders 119, 136, 148, 168 and 189 were measured,

corresponding to the central wavenumbers 2685.0, 3068.0, 3339.0, 3790.0, and 4265.0 cm^{-1}, respectively. The optical depths have been derived by averaging the transmittances with a sampling of 3 km, and deriving for each tangent height the equivalent optical depth rescaled by the occultation path. Each optical depth has been determined simultaneously with the abundances of the gases detectable in each order; hence a full retrieval is used. Each spectrum has been processed with the Planetary Spectrum Generator (PSG[46]) forward model and a retrieval scheme based on Optimal Estimation in a Gauss-Newton iterative scheme. Optical depth is derived for each tangent altitude, and is compared to the extinction of water ice with different particle sizes (top panel of Figure 9). This figure shows that the detached layer observed by NOMAD at 40-50 km can be well reproduced by a water ice cloud with particle sizes between 0.1 and 1 μm.

Aerosol properties from TIRVIM solar occultation data were retrieved from 20 wavenumbers in the spectral range of 1500−4500 cm^{-1} chosen outside of strong gas absorption bands. The procedure to obtain transmittances from the TIRVIM dataset is straightforward. This channel is operated continuously, and therefore remains very stable during an occultation. Slant optical depth is calculated as $\tau_\nu(L) = -\ln(T(L))$, where T is the transmittance over the line of sight L. Vertical profiles of extinction are retrieved using the standard 'onion peeling' method in Fedorova et al.[55]. Further steps involve Mie modelling of the spectral dependence of the extinction coefficient assuming known optical properties for the aerosols[56,57] fit to the experimental data to retrieve vertical profiles of the size distribution and number density as described in Fedorova, et al. [58]. A log-normal size distribution[59] of the aerosol particles with a width (the effective variance) of 0.3 was assumed. To distinguish between water ice and dust particles, we apply the optimal estimation retrieval scheme independently for both types, and make the decision based on the fit quality (Figure 10). The algorithm is able to retrieve the number density (typically ~1 particles cm^{-3}), and the effective radius (1–1.5 μm).

Competing interest

The authors declare no competing financial interests.

Data availability

The datasets generated by the NOMAD and ACS instruments and analysed during the current study will be available in the ESA PSA repository, https://archives.esac.esa.int/psa, after the proprietary period. The datasets directly used in this study, and especially the data used for the figures, are available from the corresponding author upon reasonable request.

Code availability

The codes used to calculate the dust/aerosols optical depths shown in figure 1 are available upon request to the corresponding author. The code used to inverse the NOMAD and ACS spectra and derive density profiles, have been favourably compared to the Planetary Spectrum Generator (PSG) tool which can be accessed at https://psg.gsfc.nasa.gov/ and which is part of this study. A version of the retrieval code is available at https://psg.gsfc.nasa.gov/helpatm.php#retrieval

Additional information

Reprints and permissions information available at www.nature.com/reprints

References

3 Fedorova, A. *et al.* Water vapor in the middle atmosphere of Mars during the 2007 global dust storm. *Icarus* **300**, 440-457 (2018).

7 Vandaele, A. C. *et al.* NOMAD, an integrated suite of three spectrometers for the ExoMars Trace Gas mission: technical description, science objectives and expected performance. *Space Sci. Rev.* **214:80**, doi.org/10.1007/s11214-11018-10517-11212, doi:https://doi.org/10.1007/s11214-018-0517-2 (2018).

8 Korablev, O. *et al.* The Atmospheric Chemistry Suite (ACS) of three spectrometers for the ExoMars 2016 Trace Gas Orbiter. *Space Sci. Rev.* **214: 7**, https://doi.org/10.1007/s11214-11017-10437-11216 (2018).

36 Neefs, E. *et al.* NOMAD spectrometer on the ExoMars trace gas orbiter mission: part 1—design, manufacturing and testing of the infrared channels. *Applied Optics* **54**, 8494-8520, doi:http://dx.doi.org/10.1364/AO.54.008494 (2015).
37 Patel, M. R. *et al.* The NOMAD spectrometer on the ExoMars Trace Gas Orbiter mission: part 2—design, manufacturing and testing of the ultraviolet and visible channel. *Applied Optics* **56**, 2771-2782, doi:https://doi.org/10.1364/AO.56.002771 (2017).
38 Svedhem, H. *et al.* The ExoMars Trace Gas Orbiter. *Space Sci. Rev.* **214**, (in press) (2018).
39 Nevejans, D. *et al.* Compact high-resolution space-borne echelle grating spectrometer with AOTF based on order sorting for the infrared domain from 2.2 to 4.3 micrometer. *Applied Optics* **45**, 5191-5206 (2006).
40 Titov, D. V. *et al.* Venus Express: Scientific Goals, Instrumentation and Scenario of the Mission. *Cosmic Res.* **44**, 334-348 (2006).
41 Korablev, O. *et al.* SPICAM IR acousto-optic spectrometer experiment on Mars Express. *J. Geophys. Res.* **111**, 1-17 (2006).
42 Formisano, V. *et al.* The Planetary Fourier Spectrometer (PFS) onboard the European Mars Express mission. *Planet. Space Sci.* **53**, 963-974 (2005).
43 Trompet, L. *et al.* Improved algorithm for the transmittance estimation of spectra obtained with SOIR/Venus Express. *Applied Optics* **55**, 9275-9281, doi:http://dx.doi.org/10.1364/AO.55.009275 (2016).
44 Lemoine, F. G. *et al.* An improved solution of the gravity field of Mars (GMM-2B) from Mars Global Surveyor. *J. Geophys. Res.* **106**, 23,359–323,376 (2001).
45 Millour, E. *et al.* (2015).
46 Villanueva, G., Smith, M., Protopasa, S., Faggi, S. & Mandell, A. M. Planetary Spectrum Generator: an accurate online radiative transfer suite for atmospheres, comets, small bodies and exoplanets. *J. Quant. Spectrosc. Radiat. Transfer* **217**, 86-104 (2018).
47 Devi, V. M. *et al.* Line parameters for CO_2- and self-broadening in the nu3 band of $HD^{16}O$. *J. Quant. Spectrosc. Radiat. Transfer* **203**, 158-174 (2017).
48 Devi, V. M. *et al.* Line parameters for CO_2- and self-broadening in the nu1 band of $HD^{16}O$. *J. Quant. Spectrosc. Radiat. Transfer* **203**, 133-157 (2017).
49 Gordon, I. E. *et al.* The HITRAN2016 Molecular Spectroscopic Database. *J. Quant. Spectrosc. Radiat. Transfer* **203**, 3-69, doi:doi:10.1016/j.jqsrt.2017.06.038 (2017).
50 Liuzzi, G. *et al.* Methane on Mars: new insights into the sensitivity of CH4 with the NOMAD/ExoMars spectrometer through its first in-flight calibration. *Icarus* **321**, 671-690, doi:doi:10.1016/j.icarus.2018.09.021 (2018).
51 Rodgers, C. D. *Inverse methods for atmospheric sounding: Theory and practice*. (University of Oxford, 2000).
52 Maltagliati, L. *et al.* Annual survey of water vapor vertical distribution and water–aerosol coupling in the martian atmosphere observed by SPICAM/MEx solar occultations. *Icarus* **223**, 942-962 (2013).
53 Levenberg, K. A method for the solution of certain non-linear problems in least squares. *Quarterly Journal of Applied Mathematics*, 164-168 (1944).
54 Marquardt, D. An Algorithm for Least-Squares Estimation of Nonlinear Parameters. *Journal of the Society for Industrial and Applied Mathematics* **11**, 431-441 (1963).
55 Fedorova, A. *et al.* Solar infrared occultation observations by SPICAM experiment on Mars-Express: Simultaneous measurements of the vertical distributions of H_2O, CO_2 and aerosol. *Icarus* **200**, 96-117 (2009).
56 Warren, S. G. & Brandt, R. E. Optical constants of ice from the ultraviolet to the microwave: A revised compilation. *J. Geophys . Res* . **113**, D14220, doi:doi:10.1029/2007JD009744 (2008).
57 Wolff, M. J. *et al.* Wavelength dependence of dust aerosol single scattering albedo as observed by CRISM. *J. Geophys. Res.* **114**, E00D04, doi:10.1029/2009JE003350 (2009).

58 Fedorova, A. *et al.* Evidence for a bimodal size distribution for the suspended aerosol particles on Mars. *Icarus* **231**, 239-260, doi:http://dx.doi.org/10.1016/j.icarus.2013.12.015 (2014).

59 Hansen, J. E. & Travis, L. D. Light Scattering in Planetary Atmospheres. *Space Sci. Rev.* **16**, 527-610 (1974).

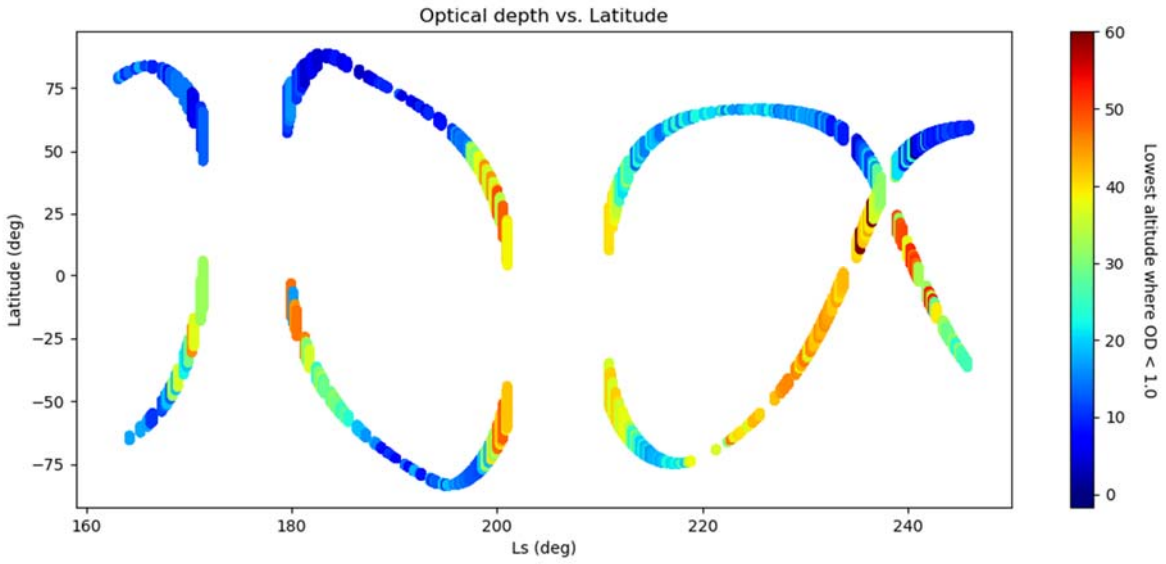

Figure 4: Continuum optical depth vs latitude and Ls. The colour denotes the lowest altitude at which the optical depth is less than 1.0, i.e. the lowest altitude where sunlight can still penetrate the atmosphere easily. There is a strong latitudinal dependence, where northern and southern high latitudes are relatively clear until the line of sight drops below 10-15km (blue and dark blue) – except during the Ls = 200° – 240° period where the global dust storm appears to have raised this altitude to 20-25km (light blue and cyan)

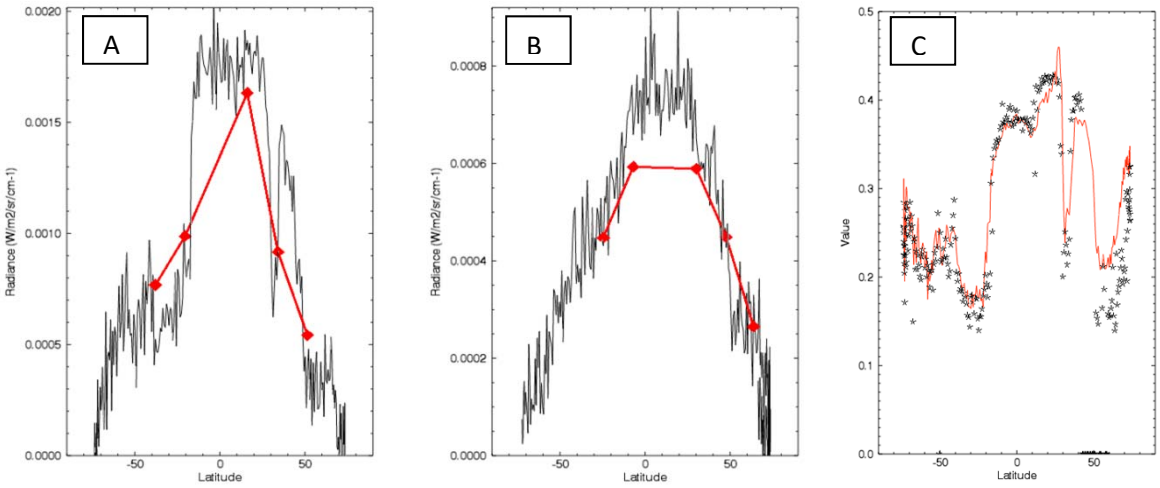

Figure 5: Impact of the dust storm on NOMAD LNO nadir observations. The calibrated radiance at 2.3 μm is shown for two orbits before (Panel A) and during (Panel B) the dust event as a function of the latitude. In red, the comparison to a radiative transfer model is also presented. The dust opacity before the global dust storm is τ=0.46 at 3 μm, while during the event, there is an increase by at least of a factor 10 (τ=4.6). Panel C shows the surface albedo, in black OMEGA albedo at 2.33 μm (order 190), in red TES bond albedo scaled to the OMEGA one.

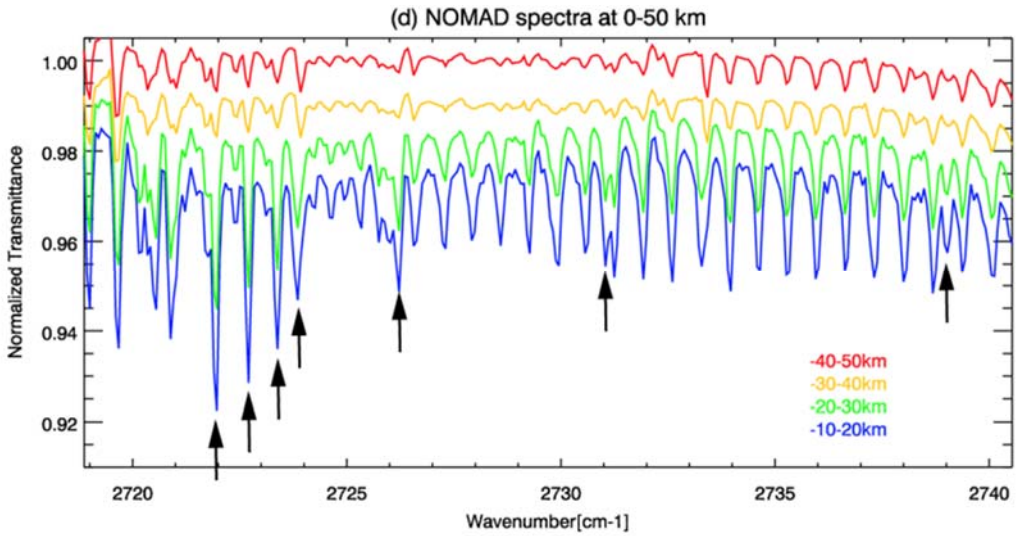

Figure 6: Atmospheric transmittances measured by NOMAD during the storm (Ls = 196.64° – Lat = 51° – Lon = 148°E) showing HDO absorption features (arrows) appearing at tangent heights up to 50 km; most of the other absorption features originate from CO_2.

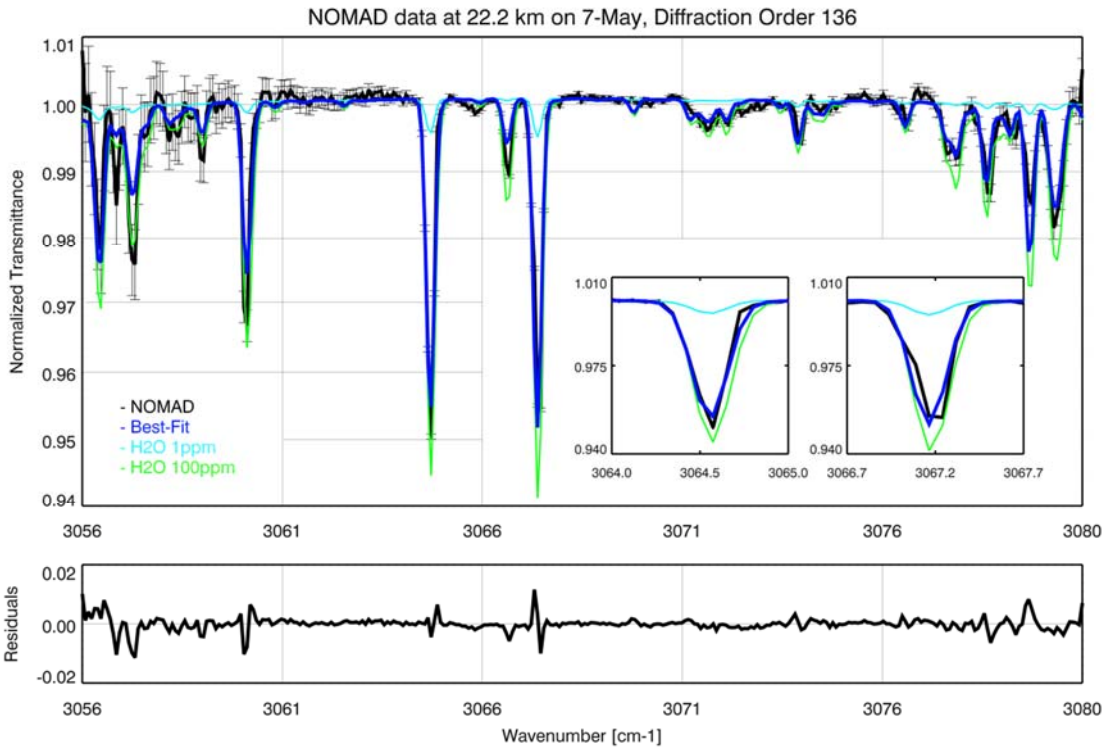

Figure 7: Example of results of the H_2O retrieval from NOMAD. Top panel: black: transmittance measured at the tangent height of 22.2 km; blue: best fit; cyan and green: different simulations with 1 ppm and 50 ppm water respectively. Bottom panel: residuals between the observation and the best fit.

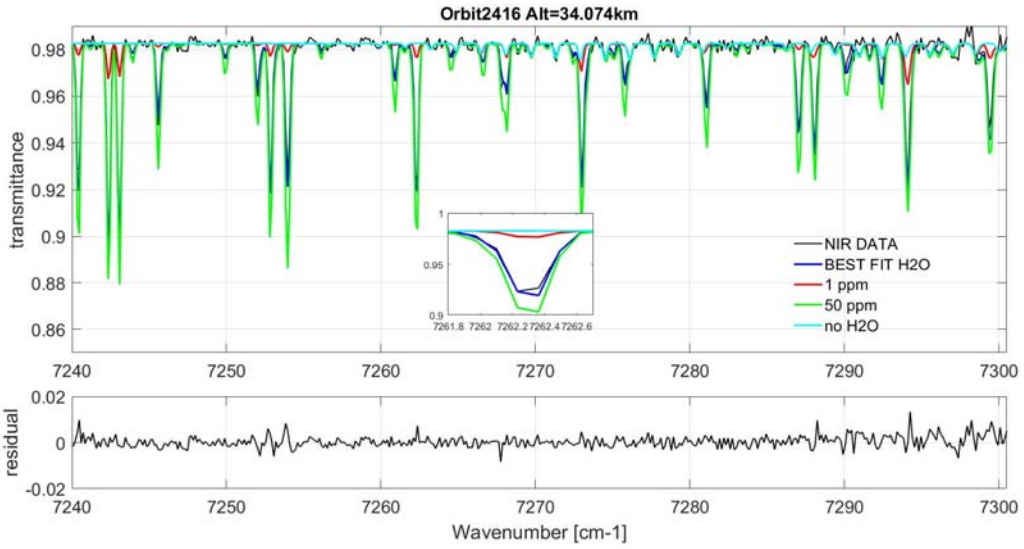

Figure 8: Example of results of the H_2O retrieval from ACS NIR. Top panel: black: transmittance measured at the tangent height of 34.07 km; blue: best fit; cyan, red, and green: different simulations with no water, 1 ppm and 50 ppm water respectively. Bottom panel: residuals between the observation and the best fit.

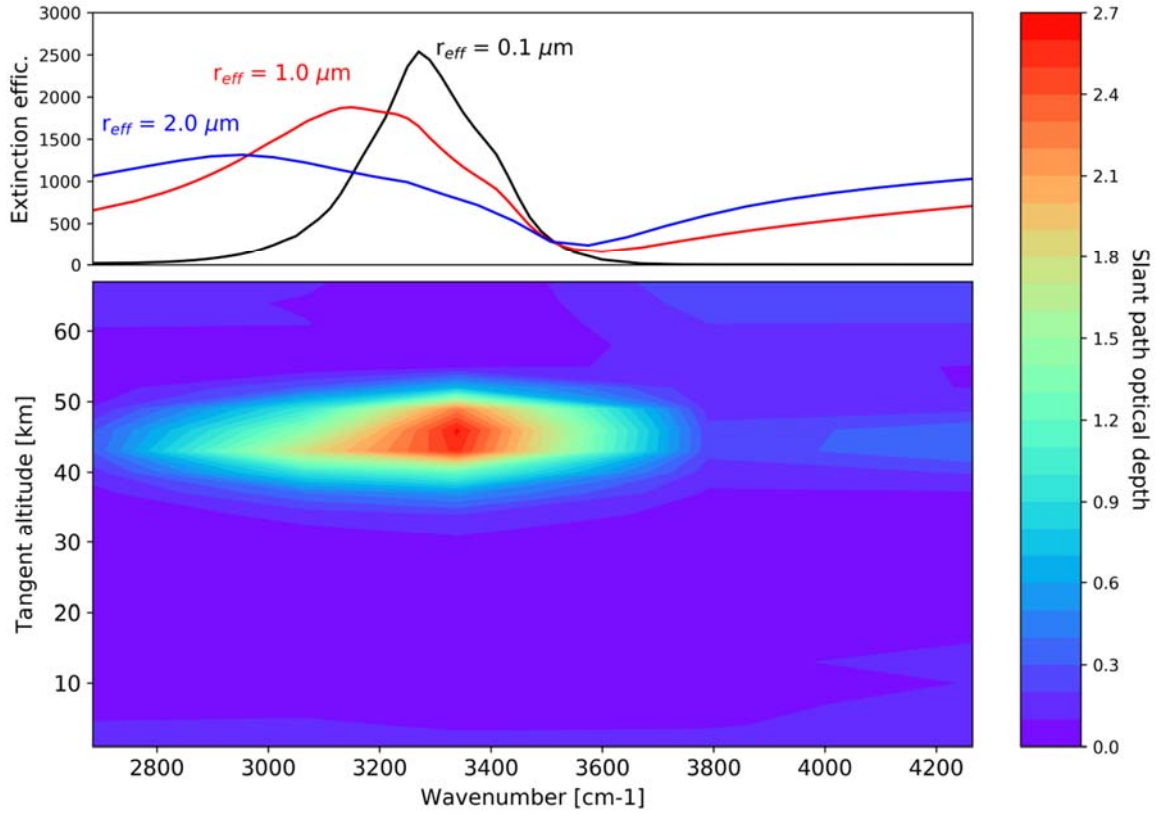

Figure 9: Extinction of water ice with different particle sizes (top panel) and slant optical depth for the solar occultation performed by NOMAD before the dust storm, derived from orders 119, 136, 148, 168 and 189. The occultation has been performed on May 7th between 05.40 and 05.46 UTC (local time 18h), and covers the latitude range 44° N to 57° N and the longitude range -122.6° E to -121.4° E.

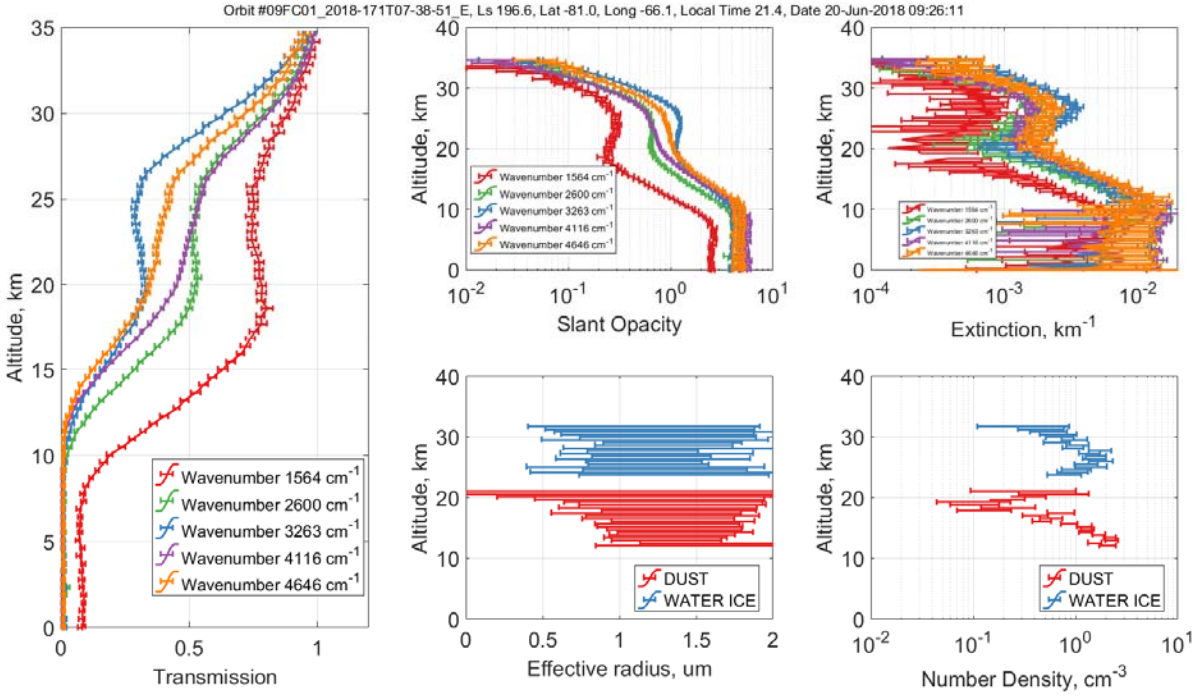

Figure 10: Illustration of independent retrieval of dust and water ice aerosol from the TIRVIM dataset for a typical southern hemisphere occultation (20.06.2018; Lat 81°N; Lon -66°E; egress): a selection of transmission profiles at 5 wavelengths, corresponding slant opacities and extinction profiles (top), retrieved effective radius (r_{eff}) in µm and aerosol number density in cm^{-3} (bottom). The occultation has been performed on June 20th at orbit 2556 (local time 21:25), and covers the latitude range 81°N to 82°N and the longitude range -67°E to -60°E. The observation corresponds to the MIR H_2O-HDO profiles during the dust storm (yellow curves of Fig.3). The water ice and dust are well distinguished using the 3 µm water ice absorption band (wavenumber 3263 cm^{-1} in the figure). In this case the water ice cloud is detected at 25-30 km.

Table 1: Overview of the NOMAD and ACS observations of H_2O and HDO used and shown in this study

Instrument	Date (UT)	Solar Longitude	Latitude	East Longitude	Local solar time	Diffraction orders	Note
ACS-MIR	2th May 2018	168.75°	39 ° S – 43°S	From 156° to -157°	17.7	224 MIR (H_2O) 224 MIR (HDO)	Before global dust storm
NOMAD SO	7th May 2018	171.45°	43° – 68°	From -122° to -115°	18.3	168 (H_2O) 136 (H_2O) 119 (HDO)	Before global dust storm
ACS-NIR	6th June 2018	188.28°	77.5°N	-173°	16.8	56 NIR (H_2O)	In the beginning of global dust storm
ACS-NIR	6th June 2018	188.62°	68.2°S	161.6°	5.4	56 NIR (H_2O)	In the beginning of global dust storm
ACS-NIR	6th June 2018	188.75°	76.4°N	-100.5°	16.9	56 NIR (H_2O)	In the beginning of global dust storm
ACS-NIR	7th June 2018	189.19°	70°S	176°	5.3	56 NIR (H_2O)	In the beginning of global dust storm
ACS-NIR	7th June 2018	189.41°	74.8°N	-141.3°	17.0	56 NIR (H_2O)	In the beginning of global dust storm

ACS-NIR	8th June 2018	189.67°	71.3°S	-112.3°	5.2	56 NIR (H_2O)	In the beginning of global dust storm
ACS-NIR	8th June 2018	189.9°	73.8°N	-68°	17.0	56 NIR (H_2O)	In the beginning of global dust storm
ACS-NIR	8th June 2018	190.05°	72.4°S	16.8°	5.1	56 NIR (H_2O)	In the beginning of global dust storm
ACS-NIR	8th June 2018	190.5°	73.8°S	88.11°	4.9	56 NIR (H_2O)	In the beginning of global dust storm
ACS-MIR-TIRVIM	20th June 2018	196.64°	80 ° S – 83°S	From -68° to -52°	21.5	224 MIR (H_2O) 224 MIR (HDO)	During global dust storm
NOMAD SO	20th June 2018	196.64°	51° – 59°	From -148° to -148°	17.3	168 (H_2O) 134 (H_2O) 121 (HDO)	During global dust storm